Applied Surface Science 622 (2023) 156951

Contents lists available at ScienceDirect

Applied Surface Science

journal homepage: www.elsevier.com/locate/apsusc

Full Length Article

Designing layered V_2O_3@C with stable oxygen defects via UV-curing technology for high-performance Zn-ion hybrid supercapacitors

Hanqin Liang [a,1], Bo Hai [b,1], Yuan Wang [a], Kuangyu Han [a], Ning Miao [a], Jinchang Wang [a], Yulian Pang [c], Hang Wei [a,*], Zhiming Shi [d], Haibin Chu [a,*], Yingquan Zou [c,*]

[a] College of Chemistry and Chemical Engineering, Inner Mongolia Engineering and Technology Research Center for Catalytic Conversion and Utilization of Carbon Resource Molecules, Inner Mongolia University, Hohhot 010021, China
[b] Department of Science, Inner Mongolia Agricultural University, Hohhot 010021, China
[c] Department of Applied Chemistry, College of Chemistry, Beijing Normal University, Beijing 100088, China
[d] State Key Laboratory of Luminescence and Applications, Changchun Institute of Optics, Fine Mechanics and Physics, Chinese Academy of Sciences, Changchun 130033, China

ARTICLE INFO

Keywords:
UV-curving technology
V_2O_3@C
Oxygen defects
Zinc-ion hybrid supercapacitor

ABSTRACT

Zn-ion hybrid supercapacitors (ZHSCs) have attracted enormous interest recently due to the perfect integration of superb energy density and power density. However, they are still bottlenecked by the low specific capacities of inadequate carbon cathodes. Herein, a layered carbon cathode embedded with oxygen-deficient V_2O_3 (O_d-V_2O_3@C) is prepared via a UV-curving technology, which endows the super uniform anchoring of O_d-V_2O_3 into the carbon matrix. The stabilities of the crystal phase and oxygen vacancies of O_d-V_2O_3 are significantly improved due to the O_d-V_2O_3 being tightly immobilized in the carbon. Density functional theory (DFT) calculations reveal that introduced oxygen defects enhance the electronic conductivity and reduce the adsorption energy of Zn^{2+}, thus increasing the storage performance. The O_d-V_2O_3@C features both reversible faradic reactions and electric double-layer capacitance, leading to a large capacity of 200.3 mA h g^{-1} even at 20 A g^{-1} with a long cycle life (remains 80.6% after 12,000 cycles). Impressively, the ZHSC delivers an exceptional high energy density of 195.0 Wh kg^{-1} (363.1 W kg^{-1}) and a power density of 13959.4 W kg^{-1} (162.9 Wh kg^{-1}). This work provides a novel strategy to construct advanced carbon-coated ultra-small metal-oxides compounds, which can be applied to other energy storage fields.

1. Introduction

A hybrid supercapacitor (HSC) integrates the advantages of both the high energy density of battery and the advanced power density of supercapacitor and has become one of the most viable choices for future large devices and portable electronic devices [1]. Therefore, HSCs have been widely investigated and achieved potential development. Different metal hybrid supercapacitors have other charge carriers, such as Li^+ [2], Na^+ [3], K^+ [4], and Zn^{2+} [5]. Among them, some shortcomings exist in the practical application of alkali metal ions. For example, the organic electrolyte is often used when lithium-ion is the charge carrier, and alkali metals are prone to severe redox reactions with water/air, leading to serious safety risks [6]. The alkali metal HSC not only has a great demand for manufacturing conditions and costs but also exhibits potential environmental pollution. Compared with alkali metal ions, Zn^{2+} owns the smaller radius and higher electrode potential (-0.76 V vs. RHE) [7], so it can be used as the charge carrier of water-based HSCs, which is safe, environmentally friendliness, and low-cost. Moreover, the conductivity of the aqueous electrolyte (~1 S cm^{-1}) is much higher than that of the non-aqueous electrolyte (1–10 mS cm^{-1}). Thus, it is expected that the Zn-ion hybrid supercapacitor (ZHSC) has a more significant power density. Even so, due to the limited energy storage mechanism of most carbon-based electrodes (AC) based on simple physical adsorption/desorption processes [8], AC//Zn ZHSCs still suffer from low energy density currently [9]. By contrast, pseudocapacitive materials combine double-layer capacitance and reversible faradic reaction mechanisms [10], which provide higher energy storage capacity for ZHSCs. Therefore, it is of great practical significance to develop new pseudocapacitive

* Corresponding authors.
E-mail addresses: weihang@imu.edu.cn (H. Wei), chuhb@imu.edu.cn (H. Chu), zouyq@bnu.edu.cn (Y. Zou).
[1] These authors contributed equally to this work.

https://doi.org/10.1016/j.apsusc.2023.156951
Received 2 February 2023; Received in revised form 28 February 2023; Accepted 3 March 2023
Available online 7 March 2023

materials with composite energy storage mechanisms.

In recent years, many pseudocapacitive materials have been developed, including heteroatom-doped carbon [11], MXenes [12], polymers [13], and transition metal compounds (TMCs) [14]. For example, Lu et al. [15] proposed layered B/N co-doped porous carbon, and the Zn// B/N carbon showed exceptional energy/power density of 86.8 Wh kg^{-1}/ 12.2 kW kg^{-1}; Wang et al. [16] designed an MXenes-rGO electrode, which achieved a prolonged cycling lifetime of 75,000 cycles with a 95% capacity retention. Nevertheless, TMCs materials with multiple metal valences and high theoretical capacity are considered the most promising electrodes for the practical application among numerous pseudocapacitive materials in ZHSCs [17]. The critical problem is how to figure out the slow ion migration kinetics caused by phase conversion during the charging and discharging of battery-type TMCs materials. Based on the above reason, only a few TMCs materials, such as RuO_2 [18] and TiN [19], have been applied to Zn//capacitor-type electrodes ZHSCs at present. Typical Zn^{2+} storage materials, such as manganese oxide [20] and vanadium oxide [21], have higher capacity, but achieving higher power density performance by obtaining the characteristics of capacitive materials is still worth discussing. As we know, smaller nano TMCs materials [22] display less resistance, faster ions, and electron transfer rates. They can slow down the volume changes and inhomogeneity during the phase transition process, which are very suitable for application as capacitor-type materials in ZHSCs. Nevertheless, monodisperse ultra-small nanomaterials are very easy to agglomerate, and the synthesis process is usually complicated, which is difficult for large-scale production.

UV-curing technology refers to a kind of curing technology in which substances containing photoactive groups undergo a series of polymerization reactions under UV radiation, so as to cross-link to form a macromolecular network [23]. UV-curing technology can be divided into free radical curing and cationic curing according to the different initiators. Compared with cationic curing, free radical photocuring is not only fast (the fastest polymerization speed is less than 0.1 s) and cheap, but also less sensitive to alkali and moisture. The free radical strategy reduces the adverse impact of the addition of non-photosensitive materials on the curing effect, so it is beneficial to the anchoring of doped components in the UV-curing system. Particularly, acrylates as UV-curable monomers can be miscible with water and common organic solvents, which are mild solvents and can dissolve most inorganic salts. Moreover, adding an appropriate amount of inorganic salts will not significantly affect the UV-curable properties. Taking advantage of the unique properties of the UV-sensitive monomers, the inorganic salts can be dissolved in monomers avoiding the UV light. After the inorganic salts dissolve and uniformly disperse at the molecular scale, the mixture liquid can be cured instantaneously with UV exposure. Finally, the uniformly distributed ultra-small nanomaterials embedded in carbon can be obtained after pyrolysis of the cured solid precursor [24]. The UV curing technology simplifies the preparation process and inhibits the secondary agglomeration of ultra-small nanomaterials, which can broaden the potential application prospects of TMCs materials in Zn// capacitor-type ZHSCs.

Herein, the mixtures of 2-hydroxyethyl methacrylate (HEMA), poly (ethylene glycol) diacrylate (PEGDA), and pentaerythritol triacrylate (PETA) are simultaneously used as dispersed substrates, and UV-sensitive monomers. V_2O_5 colloidal solution act as a vanadium source. Then a new generation of layered carbon embedded with oxygen-deficient nano V_2O_3 (O_d-V_2O_3@C) cathodes is finely designed and prepared through UV-curing technology and a pyrolysis process. The O_d-V_2O_3 provides abundant defects and multiple active sites, which offer more Zn^{2+} diffusion pathways and rapid ions transport kinetics, thus resulting in an improved capacity and cycling stability for O_d-V_2O_3@C. Consequently, pairing the O_d-V_2O_3 cathode with the Zn anode yields an aqueous ZHSC, achieving an impressive specific capacity of 200.3 mA h g^{-1} even at 20 A g^{-1} with long cycle life (remains 80.6% after 12,000 cycles). The Zn//O_d-V_2O_3@C device delivers an exceptional high energy density of 195.0 Wh kg^{-1} at 363.1 W kg^{-1} and a power density of 13959.4 W kg^{-1} at 162.9 Wh kg^{-1}, indicating significant potential for next-generation high-performance ZHSC.

2. Materials and methods

2.1. Preparation of O_d-V_2O_3@C

The mixture of HEMA (45 wt%), PEGDA (50 wt%), and PETA (5 wt %) are simultaneously used as dispersed substrates and UV-sensitive monomers. The three monomers have different amounts of unsaturated bonds. Therefore, the viscosity of the solvent and the adhesive degree of the UV-curing can be adjusted by adjusting the mixing quantity of the three monomers. In this case, 0.3 g commercial V_2O_5 was mixed with 0.15 g water and stirred until a stable colloidal solution was formed. Then, the V_2O_5 colloidal solution and 0.18 g phenylbis(2,4,6-trimethylbenzoyl)phosphine oxide (initiator) were dissolved in 6 g acrylate monomers in a dark room. The precursor solution was exposed to UV light, and the liquid material transformed into solid material instantaneously. The UV-curing polymerization mechanism is shown in Fig. S1. The V_2O_3@C could be obtained after pyrolysis of the above solid precursor in a tubular furnace under a nitrogen atmosphere for 400 °C for 1 h and 700 ℃ for 1 h with a heating rate of 5 °C min^{-1}. After that, O_d-V_2O_3@C can be prepared by further calcinating V_2O_3@C under H_2 for 1 h at 400 °C.

2.2. Characterization

The crystalline phases of the samples were identified by X-ray Bruker D8 Advance diffractometer using Cu Kα irradiation (λ = 1.5406 Å). The morphology and size of the composites were observed by Hitachi s-4800 (SEM) and FEI Tecnai F20 (TEM). High-resolution transmission electron microscopy (HRTEM) and energy dispersive spectroscopy (EDS) images were captured using an emission transmission electron microscope. Thermogravimetric analysis (TGA) was performed on the PerkinElmer TGA 4000 equipment with a heating rate of 10 °C min^{-1} under an air environment. X-ray photoelectron spectroscopy (XPS) experiments were conducted at a Thermo Scientific ESCALAB Xi + using Al Kα as the excitation source. Electron paramagnetic resonance (EPR) analyses were collected on a Bruker E-500 spectrometer.

2.3. Electrochemical measurement

The slurry was prepared by V_2O_3-based materials (70 wt%) mixed with Super P (20 wt%) and polyvinylidene fluoride (10 wt%) in N-methyl-2-pyrrolidone. Then the resulting slurry was coated on carbon paper and dried. The mass loading of active materials was 1.2–1.5 mg cm^{-2}. The aqueous and pouch ZHSCs were assembled with a V_2O_3-based cathode and Zn foil anode, in which 3 M $Zn(CF_3SO_3)_2$ solution and Whatman filter paper were used as electrolyte and separator, respectively.

All electrochemical tests containing cyclic voltammetry (CV), galvanostatic charge–discharge (GCD) and the Galvanostatic intermittent titration technique (GITT) were performed at 0.2–1.6 V on the NEWARE battery tester. The potential range for CV and GCD tests was fixed. The GITT was conducted to determine the Zn^{2+} diffusion coefficient within a 10 min charge/discharge and followed by a 60 min relaxation at a current density of 100 mA g^{-1}. The electrochemical impedance spectroscopy (EIS) was tested on a CHI 760e with frequencies from 100 kHz to 10 mHz. The energy density (E, Wh kg^{-1}) and power density (P, W kg^{-1}) of the ZHSCs were calculated via the equation [25].

$E = C^*\Delta V/2$; $P = 3600^*E/\Delta t$;

where C (mAh g^{-1}) is the specific capacity, ΔV (V) represents the voltage window, and Δt (s) indicate the discharge time.

2.4. Calculations

The first-principles [26] was employed to perform all spin-polarization density functional theory (DFT) calculations within the generalized gradient approximation (GGA) using the Perdew-Burke-Ernzerhof (PBE) [27] formulation. The projected augmented wave (PAW) potentials [28] have been chosen to describe the ionic cores and take valence electrons into account using a plane wave basis set with a kinetic energy cutoff of 400 eV. Partial occupancies of the Kohn-Sham orbitals were allowed using the Gaussian smearing method and a width of 0.05 eV. The electronic energy was considered self-consistent when the energy change was more minor than 10^{-5} eV. A geometry optimization was considered convergent when the energy change was smaller than 0.05 eV $Å^{-1}$. In this case, the U correction is used for V atoms. The Brillouin zone integration is performed using 3 × 3 × 2 Monkhorst-Pack k-point sampling for a structure. Finally, the adsorption energies (E_{ads}) were calculated as $E_{ads} = E_{ad/sub}-E_{ad}-E_{sub}$, where $E_{ad/sub}$, E_{ad}, and E_{sub} are the total energies of the optimized adsorbate/substrate system, the adsorbate in the structure, and the clean substrate, respectively.

3. Results and discussions

3.1. Synthesis and characterization of O_d-V_2O_3@C

The layered O_d-V_2O_3@C were fabricated through a facile UV-curving and a pyrolysis process (Fig. 1), in which the UV-curing polymerization mechanism is shown in Fig S1. It is generally accepted that structures and electrical conductivity of electrodes play a crucial role in ion diffusion and boosting the capacity. V_2O_3 is inherently more conductive than most transition metal oxides (the resistance of bulk V_2O_3 is just about 10 Ω) [29], and the unique open tunnel structure facilitates the rapid migration of Zn^{2+} [30]. In this case, the V_2O_3 with abundant oxygen defects is highly dispersed in the layered carbon. Thus, the conductivity and the diffusion of Zn^{2+} can be further motivated. What is worth mentioning, the low-valence state of vanadium and oxygen defects in the O_d-V_2O_3@C exhibit exceptional stability, which can remain intact in the air due to the tight coating of carbon, ensuring the improved electrochemical performance of O_d-V_2O_3@C in ZHSC.

The XRD patterns confirmed the formation of V_2O_3 (JCPDS No. 34–0187) (Fig. 2a) [31]. The O_d-V_2O_3@C was obtained from further pyrolysis of V_2O_3@C in the H_2 atmosphere without any change in phase composition. In addition, no peak of carbon was found, indicating the presence of amorphous carbon in V_2O_3@C and O_d-V_2O_3@C. As shown in the SEM image (Fig. 2b), the O_d-V_2O_3@C were composed of numerous nanosheets. The O, V, and C elements were homogeneously distributed on the nanosheets (Fig. 2c). Moreover, as characterized by EPR in Fig. 2d, the strong signal detected in O_d-V_2O_3@C was attributed to the electrons captured at the vacancy sites. It could be found that the V_2O_5 was successfully reduced to V_2O_3 during the pyrolysis of the precursor after UV-curing, and little oxygen defects were also introduced into the V_2O_3, but the content of oxygen defects significantly increases after further reduction by H_2. The microstructure of O_d-V_2O_3@C was further characterized by TEM. Fig. 2e further intuitively proves that O_d-V_2O_3@C was composed of nanosheets, and the thickness of nanosheets is just around 10–20 nm. Meanwhile, the dislocations of HRTEM marked by the dotted box (Fig. 2e) displayed small V_2O_3 grains anchored in amorphous carbon, and the interplanar distance of 0.364 nm was ascribed to the (0 1 2) plane of V_2O_3. As we know, V_2O_3 is easily oxidized to higher-state vanadium oxides in the air. However, in this case, the crystal phase and oxygen defects of O_d-V_2O_3 can be retained after 6 months in air (Fig.S2). Considering the combustion of carbon and the change of V2O3 to V2O5, the final weight of the carbon was calculated from the TGA curve (Fig.S3) as 51.8%, and the detailed calculation process was expressed in supporting information. Such tightly coated carbon layer with high content not only highly improves the stability of the structure of V_2O_3 and oxygen defects, but obviously inhibits the dissolution of the vanadium oxide cathode in the cycling processes. Besides, the novel structure is also conducive to the rapid diffusion of Zn^{2+}, which can lead to the excellent Zn^{2+} storage performance of O_d-V_2O_3@C at considerable rates.

The valence state and chemical composition of the O_d-V_2O_3@C were investigated by XPS. The XPS survey spectrum (Fig. S4) revealed that the existence of V, O, and C elements in the O_d-V_2O_3@C and V_2O_3@C samples, The C 1 s spectra in Fig. 2g includes three peaks: C–C, C-O and C = O, which locates at 284.7, 286.0, and 288.2 eV, respectively [32]. The O 1 s spectra (Fig. 2h) of both V_2O_3@C and O_d-V_2O_3@C can be fitted into four peaks, corresponding to the V-O, oxygen defects, C-O, and C = O with their peak positions at 530.6, 531.5, 532.3, and 533.2 eV, respectively [33]. The content of oxygen defects in O_d-V_2O_3@C is calculated to be 28.8 %, which is higher than that of V_2O_3@C (14.2%), consistent with the EPR results. As shown in the V 2p spectra (Fig. 2i), V 2p1/2 and V 2p3/2 spin–orbit peaks can be observed. The peaks of O_d-V_2O_3@C located at 517.3 and 524.7 eV correspond to V^{3+}, and the peaks at 516.2 and 523.6 eV are attributed to V^{2+} [34]. Compared with the V 2p spectrum of V_2O_3@C, the peaks of the O_d-V_2O_3@C sample reveal an apparent negative shift, which is caused by the oxygen defects around vanadium atoms, leading to the increased electron density near the vanadium atom. It is believed that the stable existence of oxygen defects provides abundant active sites for the adsorption and migration of Zn^{2+}, which results in the significant improvement of the electrochemical performance.

3.2. Electrochemical properties of aqueous ZHSCs device

The as-prepared O_d-V_2O_3@C presents a novel structure in which a

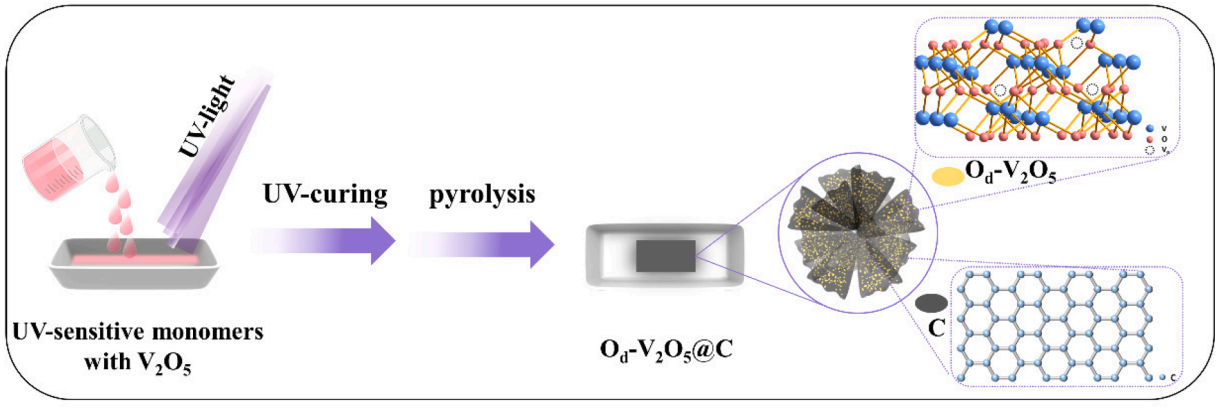

Fig. 1. Schematic illustration of the synthesis processes of O_d-V_2O_3@C.

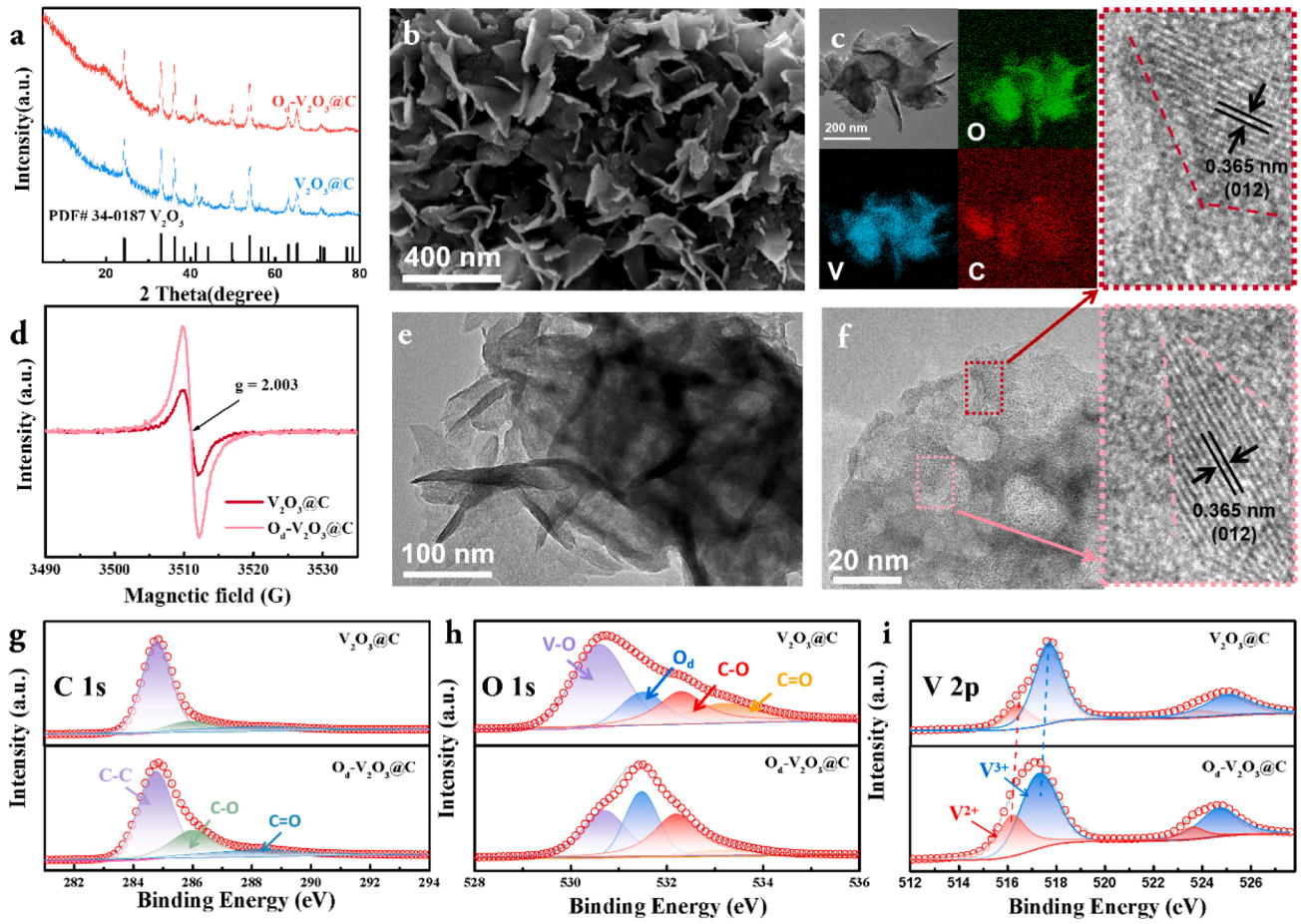

Fig. 2. (a) XRD patterns of V_2O_3@C and O_d-V_2O_3@C. (b) SEM and (c) EDS-mapping images of the O_d-V_2O_3@C. (d) Room-temperature EPR spectra of V_2O_3@C and O_d-V_2O_3@C. (e) TEM, (f) HRTEM images of the O_d-V_2O_3@C sample, and the insets are the corresponding lattice information. High-resolution XPS spectra of (g) C 1 s, (h) O 1 s, and (f) V 2p for V_2O_3@C and O_d-V_2O_3@C.

layer of carbon is embedded with oxygen-deficient nano V_2O_3 enables abundant active sites for the Zn^{2+} adsorption and short distance for electrons diffusion. Benefiting from the virtues of the O_d-V_2O_3@C cathode, the Zn//Zn$(CF_3SO_3)_2$(aq.)//O_d-V_2O_3@C and ZHSC Zn//Zn$(CF_3SO_3)_2$(aq.)//V_2O_3@C devices have been developed. Fig. 3a shows CV curves of the V_2O_3@C and O_d-V_2O_3@C electrodes at the scan rate of 50 mV s^{-1}, which suggests the ZHSCs can work well in the potential window of 0.2–1.6 V. And the similar electrochemical redox behavior indicates that more oxygen defects do not change the redox reaction of the electrode, the larger area of O_d-V_2O_3@C reveals a superior zinc storage performance than that of V_2O_3@C. The specific capacities of both ZHSCs were tested by galvanostatic charge–discharge (GCD) curves. Fig. S5 shows the O_d-V_2O_3@C cathode can reach 258.4 mAh g^{-1} at 0.5 A g^{-1}, which is much higher than that of V_2O_3@C, indicating the oxygen defects play an important role in the electrochemical properties of cathodes. Fig. 3b presents the GCD curves of O_d-V_2O_3@C cathode at 0.5–20 A g^{-1}, which show that capacity of 278.9, 270.8, 261.0, 248.7, 240.2, and 232.7 mAh g^{-1} at 0.5, 1, 2, 5, 10, and 20 A g^{-1}, respectively. The rate capability of O_d-V_2O_3@C (Fig. 3c) clearly indicates that the O_d-V_2O_3@C ZHSCs maintain sufficient stability after cycling at different rates, which also shows that the oxygen defects have sufficient stability in the O_d-V_2O_3@C cathode. Impressively, the capacity retention is as high as 83.4% at a high rate of 20 A g^{-1} (compared with 0.5A g^{-1}) demonstrating O_d-V_2O_3@C cathode exhibit excellent rate performance. Especially, the illustrations (Fig. S6) show the "IMU" logo containing 21 LED bulbs that can be lit by a pouch ZHSC in different bending states, indicating the great potential for the commercial application of ZHSCs. This result outperforms most advanced devices, such as O_d-HVO@PPY (252.6 mA h g^{-1} at 6 A g^{-1}) [35], flower-like carbon (70 mA h g^{-1} at 20 A g^{-1}) [36], and N-CNF (65 mA h g^{-1} at 20 A g^{-1}) [37], and related results are summarized in Table S1. Besides, the remarkable capacity of 161.4 mA h g^{-1} was maintained over 12,000 cycles at 20 A g^{-1} (Fig. 3d), displaying the prominent cycle stability of O_d-V_2O_3@C. Based on such excellent rate performance of O_d-V_2O_3@C cathode, this device exhibits extremely high energy (195.0 Wh kg^{-1} at 363.1 W kg^{-1}) and power density (13959.4 W kg^{-1} at 162.9 Wh kg^{-1}), and the areal Ragone plot including O_d-V_2O_3@C is presented in Fig. 3f. The obtained results are superior to the values reported in the literature (Table S1). Specifically, the power density offered by this ZHSC is very close to the most efficient supercapacitors, and the energy density even exceeds those of efficient batteries.

Density functional theory (DFT) calculations have been performed to further explore the effects of oxygen defects on the O_d-V_2O_3@C cathode performance. The structural models of V_2O_3 and O_d-V_2O_3 are established and shown in Fig. S7. The partial and total density of states (PDOS and DOS) are displayed in Fig. 4a-4b. The DOS of O_d-V_2O_3 moves to a low energy direction with the Fermi level. Thus, the bandgap (0.23 eV) of O_d-V_2O_3 is much smaller than that of V_2O_3 (0.97 eV), which demonstrates the better conductivity of O_d-V_2O_3 and faster transfer of electrons in the redox reaction. These results are favorable consistently with the increase in conductivity measured in the electrochemical impedance spectroscopy (EIS). As shown in Fig. 4c, the charge transfer resistance of the O_d-V_2O_3@C electrode is much lower than that of the V_2O_3@C electrode.

Furthermore, the reaction kinetics of O_d-V_2O_3@C has been examined through CV curves at scan rates of 1–100 mV s^{-1} (Fig. 4d). The CV shape

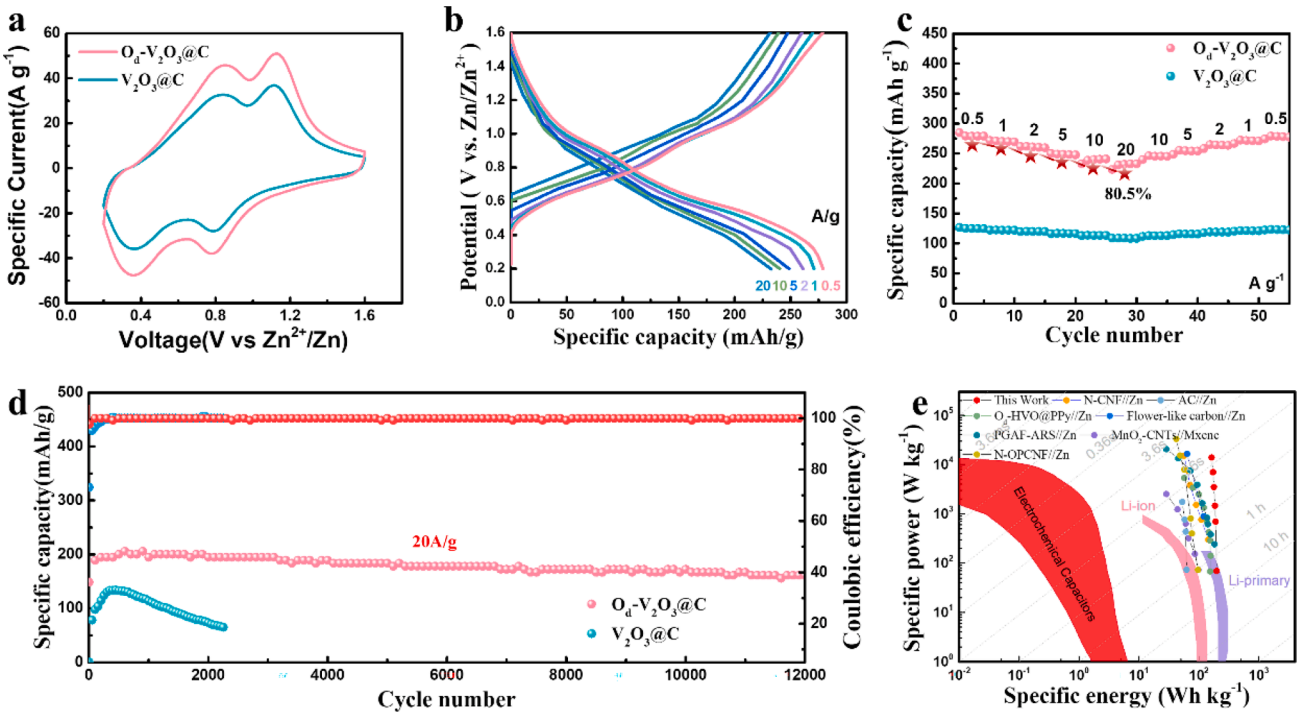

Fig. 3. (a) CV curves obtained at 50 mV s^{-1} of V_2O_3@C and O_d-V_2O_3@C. (b) Voltage profiles of O_d-V_2O_3@C for different current densities. (c) Rate performance of V_2O_3@C and O_d-V_2O_3@C at various current densities ranging from 0.5 to 20 A g^{-1}. (d) Cyclic performance and coulombic efficiency of Zn//O_d-V_2O_3@C and Zn//V_2O_3@C ZHSCs at a current density of 20 A g^{-1}. (e) Ragone plot of O_d-V_2O_3@C compared with reported cathodes of some energy storage devices [35–41].

are well retained as the scan rate increased, confirming the fast kinetics and high transfer rates of ions and electrons. The peak current (i) and scan rate (v) can be fitted by the following formula: $i = av^b$. Generally, the b value of 0.5 indicates the energy storage process is a diffusion-controlled process, while b equal to 1 represents a surface-controlled process. In this case, the b values have been calculated according to log(i), and log(v), in which peaks 1–4 were obtained as 0.64, 0.78, 0.86, and 0.77, demonstrating the synergistic behavior of diffusion control and capacitive process. To further determine the specific contribution of diffusion and capacitance behavior, the formula $i = k_1v + k_2v^{0.5}$ has been chosen and used. The capacitive- and diffusion-controlled contributions can be evaluated as the value of k_1v and $k_2v^{0.5}$, respectively. The capacitive contribution of O_d-V_2O_3@C can be calculated through plotting the curves of k_1v and potential (V). Almost 97.9% of the total stored charge (the shaded area) is achieved by the surface capacitance process at 100 mV s^{-1} (Fig. 4f). Obviously, the capacitive contribution ratio gradually increases from 72.4% to 97.9% with the increase of scan rate from 1 to 100 mV s^{-1} (Fig. 4g), demonstrating the capacitive-dominant nature and fast kinetics plays a vital role in devoting to the improved electrochemical performance. Moreover, the diffusion coefficient (D value) of O_d-V_2O_3@C was calculated as 10^{-7}-10^{-9} cm^2 s^{-1} via the GITT measurement (Fig. S8), also suggesting the fast ions diffusion of O_d-V_2O_3@C electrode.

As described above, Zn^{2+} storage in cathodes can be generally divided into diffusive components and capacitive components. Due to the unique structure of V_2O_3@C material, the capacitive element contributes more to the zinc storage process than the diffusive component. Interestingly, the capacitive contribution of the cathode can be further increased by surface chemical modification, such as the creation of oxygen defects in V_2O_3. Here, DFT calculations were also conducted to evaluate Zn^{2+} adsorption for ZHSC on the V_2O_3 model containing oxygen vacancy. Meanwhile, the adsorption of Zn^{2+} on a perfect V_2O_3 surface was also evaluated as a benchmark. As shown in Fig. 4h and S9, Gibbs free energies of Zn^{2+} adsorption are both more negative either near or slightly further away from the oxygen defect. The more robust adsorption capacity means that the presence of oxygen defects is conducive to the Zn^{2+} adsorption on the O_d-V_2O_3 surface, which enhances the Zn^{2+} storage capacity. Since oxygen defects play such an important role in zinc storage, the stability of oxygen defects will determine the cyclic stability of the O_d-V_2O_3@C. Fig. S10 shows the EPR spectra of the O_d-V_2O_3@C after 200 cycles at 0.5A g^{-1}. It can be found that the oxygen defects in O_d-V_2O_3@C are well preserved after cycling, confirming the existence of high-content amorphous carbon can effectively inhibit the loss of oxygen defects. This result is also consistent with the stable presence of lower valence state V^{3+} in O_d-V_2O_3@C in the air (Fig. S2).

3.3. Energy storage mechanism of O_d-V_2O_3@C

The electrochemical reaction mechanism of the O_d-V_2O_3@C cathode was elucidated via the ex-situ XRD patterns and XPS measurements. Due to the nature of amorphous carbon, XRD results (Fig. 5a) can only show the changes of O_d-V_2O_3 during the charging and discharging processes. The sharp diffraction peaks located after 38.5° are well-indexed to the titanium foil used as the current collector. A new phase [42] of $Zn_3(OH)_2V_2O_7{\cdot}2H_2O$ (JCPDS: 50–0570) could be observed after the first discharge and charge cycle (from point a to point c), indicating surface redox of O_d-V_2O_3 cathode. Moreover, just the most substantial peak (1 0 4) of V_2O_3 slightly moves to lower 2θ angles during the discharge (Zn^{2+} intercalation), and then returns to the original position in the charging process of Zn^{2+} deintercalation. However, the positions of other peaks, including (0 1 2) and (1 1 0), almost do not shift during the charging and discharging cycles. This observation reveals that the redox process in the cycling is reversible, and the Zn^{2+} intercalation/deintercalation in O_d-V_2O_3 has only a mild effect on the structure, which is beneficial to the stability of the O_d-V_2O_3@C. This result is caused by the following reason: Zn^{2+} storage enhancement comes more from the capacitive component, that is, from the surface redox.

Moreover, the ex-situ XPS spectra of the O_d-V_2O_3@C electrode after the second discharge and charge cycle are conducted and shown in

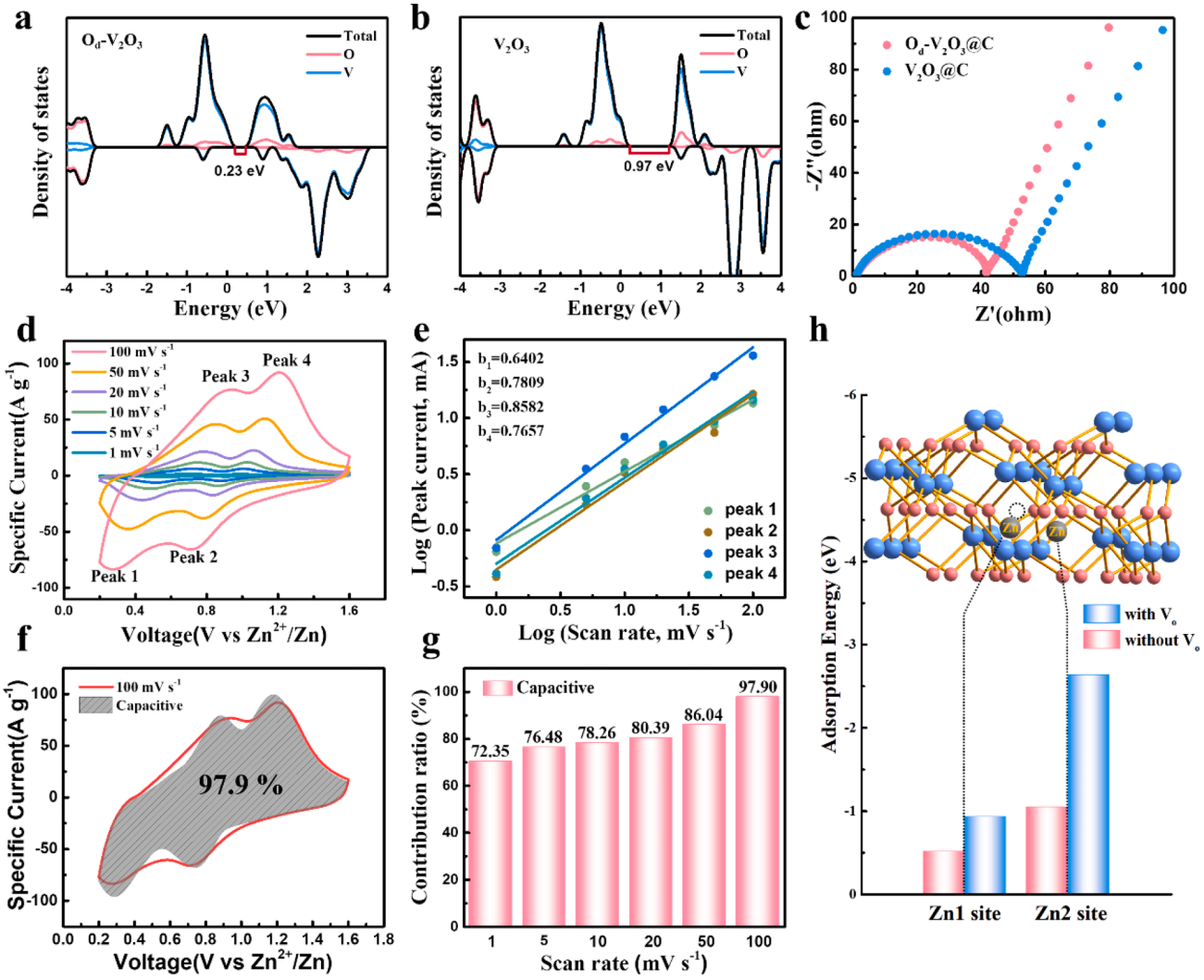

Fig. 4. The PDOS and TDOS of (a) O_d-V_2O_3@C and (b) V_2O_3@C. (c) EIS spectra of O_d-V_2O_3@C and V_2O_3@C. (d) CV curves obtained at different scan rate from 1 to 100 mV s^{-1}. (e) Fitted liner plots of log(i) and log(v) for different peaks. (f) The capacitive and diffusion contribution to the total current from the CV curve analysis at 100 mV s^{-1}. (g) Capacity contribution ratios at various scan rates. (h) The binding energy of specific binding site in V_2O_3@C and O_d-V_2O_3@C.

Fig. 5b-5d. The V2p spectrum for the pristine state in Fig. 5b displayed just V^{2+} and V^{3+}. Correspondingly, there are three valence states (2+, 3+, and 5 +) of vanadium valence states in the dischraged, or charged state, where the V^{5+} are from the $Zn_3(OH)_2V_2O_7{\cdot}2H_2O$. It also can be found that compared with the charged state, the peaks of V 2p shift slightly to lower binding energies, and the intensity of the V^{2+} signal increased during the discharge process due to the insertion of Zn^{2+}. A new broad peak appeared at 533.6 eV in the O 1 s spectrum (Fig. 5c) at the discharged state, ascribed to the H_2O molecules [43], consistent with the formation of $Zn_3(OH)_2V_2O_7{\cdot}2H_2O$. Besides, It can be noticed that oxygen defects can exist stably in the charging and discharging processes. Fig. 5d shows the Zn 2p spectrum, in which both the adsorbed Zn^{2+} and the intercalated Zn^{2+} can be observed after cycling [44], just the peak intensity changed between the discharged and charged states.

Besides, considering that the content of amorphous C in O_d-V_2O_3@C accounts for 51.8 %, the evolution of C 1 s XPS peaks deserves special attention. For a typical carbon material, the energy storage mechanism of the Zn^{2+} can be assigned to the conjoint contribution of the electrical double layers and the additional pseudocapacitance via the reversible chemical adsorption of Zn ions. As shown in Fig. 5e, the C 1 s spectra reveal that the C = O participates in highly reversible chemical reactions during the cycling processes. The peak represents to C = O bond weakening and a new peak corresponding to the C-O-Zn bond appears at 287.4 eV [45] during the discharged state, while the peak almost recovers at the charged state, indicating a reversible pseudocapacitive reaction between C = O and the Zn^{2+}. In addition, the peak at 290.5 eV belongs to the CF_2 group of PVDF [46]. Based on the above results, it can be found that the carbon matrix and O_d-V_2O_3 contribute jointly to the high capacity of ZHSCs. These above results indicate that the superior electrochemical performance of O_d-V_2O_3@C cathode comes from the super uniform anchoring structure: the synergistic effect of carbon and nano O_d-V_2O_3 improves the zinc storage capacity; the presence of oxygen defects not only improves the overall electrical conductivity, but enhances the migration and storage capacity of Zn^{2+}; the carbon-coated structure can inhibit the dissolution of reactive vanadium oxide during the cycling process, and stabilize the O_d-V_2O_3 structure including oxygen defects; the rich functional groups on the surface of carbon improve the wettability in aqueous electrolyte.

4. Conclusion

In summary, a newly designed layered carbon cathode embedded with oxygen-deficient nano V_2O_3 (O_d-V_2O_3@C) has been constructed by a UV-curing strategy and subsequent pyrolysis treatment, where endows the super uniform anchoring of O_d-V_2O_3 into carbon matrix. The combined features of carbon matrix and embedded O_d-V_2O_3 result in the O_d-

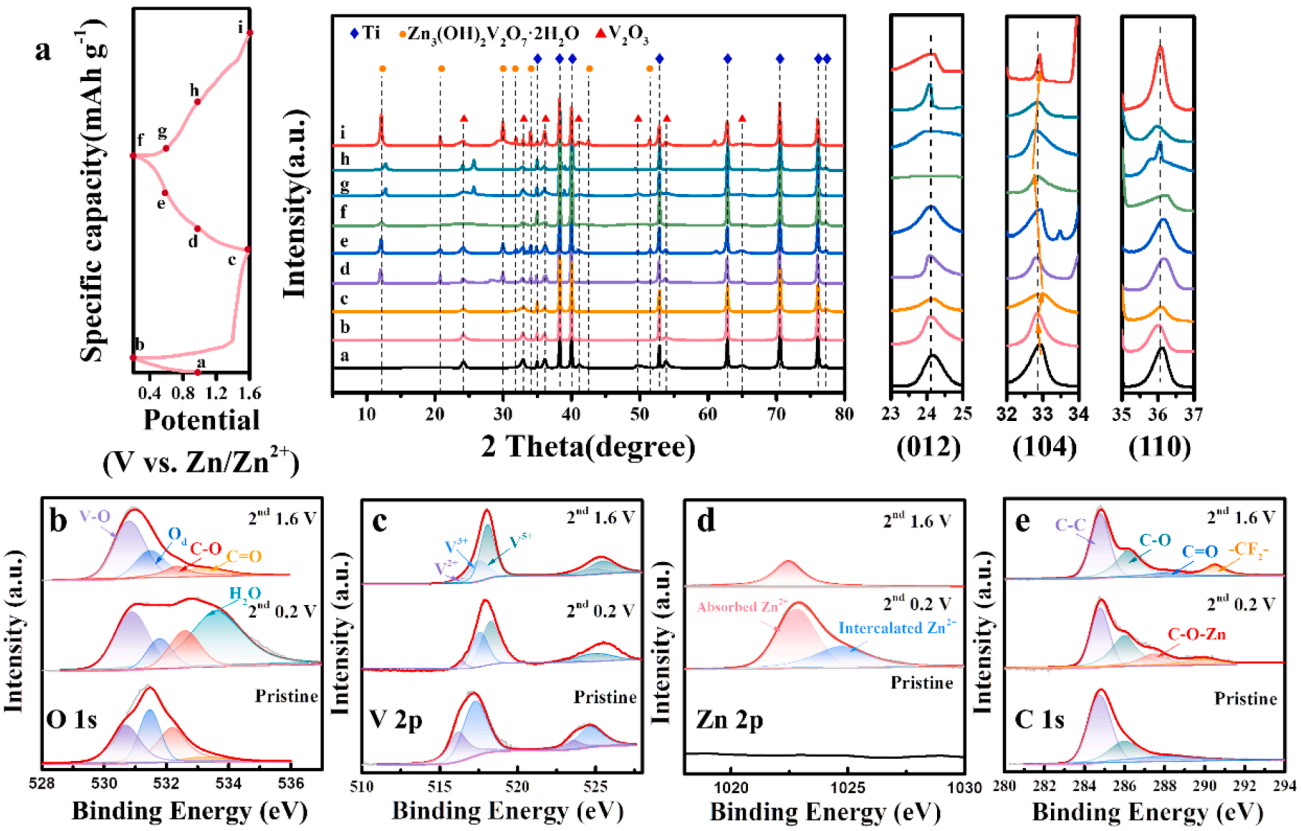

Fig. 5. (a) GCD curves in the first two cycles and ex-situ XRD patterns at different discharge/charge states of the O_d-V_2O_3@C sample. Ex situ XPS spectra of (b) O 1 s, (c) V 2p, (d) Zn 2p, and (e) C 1 s at pristine, complete discharged, and full charged states.

V_2O_3@C cathode exhibiting an outstanding energy density (195.0 Wh kg^{-1} at 363.1 W kg^{-1}), an exceptional power density (13959.4 W kg^{-1} at 162.9 Wh kg^{-1}), as well as ultralong cycling stability up to 12,000 cycles. Moreover, the correlations between the enhanced Zn^{2+} storage performance and the structure of O_d-V_2O_3@C are investigated by the theoretical simulation. DFT simulation shows that introducing the oxygen defects can effectively increase the electronic conductivity, accelerate the diffusion kinetics and reduce the adsorption energy of Zn^{2+}, leading to superior electrochemical properties. The strategy in this work provides enlightening insights for constructing a cathode with high energy density in ZHSCs areas.

Data availability

The raw data required to reproduce these findings are available upon request.

CRediT authorship contribution statement

Hanqin Liang: Methodology, Formal analysis. **Bo Hai:** Formal analysis, Data curation, Investigation. **Yuan Wang:** Validation, Writing – original draft. **Kuangyu Han:** Methodology, Investigation. **Ning Miao:** Formal analysis. **Jinchang Wang:** Investigation. **Yulian Pang:** Methodology. **Hang Wei:** Conceptualization, Resources, Writing – review & editing, Supervision, Funding acquisition. **Zhiming Shi:** Methodology. **Haibin Chu:** Supervision, Project administration, Funding acquisition. **Yingquan Zou:** Resources, Writing – review & editing.

Declaration of Competing Interest

The authors declare that they have no known competing financial interests or personal relationships that could have appeared to influence the work reported in this paper.

Data availability

Data will be made available on request.

Acknowledgments

This work was financially supported by the National Natural Science Foundation of China (21801140, 21875125, 22161033), the Natural Science Foundation of Inner Mongolia Autonomous Region of China (2022MS2010), the 111 Project (D20033), and “Grassland Talent” Program and “Grassland Talent” Innovation Team of Inner Mongolia.

Appendix A. Supplementary data

Supplementary data to this article can be found online at https://doi.org/10.1016/j.apsusc.2023.156951.

References

[1] C. Wan, W. Tian, J. Zhou, Y. Qing, Q. Huang, X. Li, S. Wei, L. Zhang, X. Liu, Y. Wu, Green anisotropic carbon-stabilized polylaminate copper oxide as a novel cathode for high-performance hybrid supercapacitors, Mater. Des. 198 (2021), 109309, https://doi.org/10.1016/j.matdes.2020.109309.
[2] G.A. dos Santos Junior, V.D.S. Fortunato, G.G. Silva, P.F.R. Ortega, R.L. Lavall, High-performance Li-ion hybrid supercapacitor based on $LiMn_2O_4$ in ionic liquid electrolyte, Electrochimica Acta 325 (2019), 134900, https://doi.org/10.1016/j.electacta.2019.134900.
[3] J. Yuan, M. Qiu, X. Hu, Y. Liu, G. Zhong, H. Zhan, Z. Wen, Pseudocapacitive vanadium nitride quantum dots modified one-dimensional carbon cages enable highly kinetics-compatible sodium ion capacitors, ACS Nano 16 (9) (2022) 14807–14818, https://doi.org/10.1021/acsnano.2c05662.
[4] S. Zhao, Z. Liu, G. Xie, X. Guo, Z. Guo, F. Song, G. Li, C. Chen, X. Xie, N. Zhang, B. Sun, S. Guo, G. Wang, Achieving high-performance 3D K^+-pre-intercalated $Ti_3C_2T_x$ MXene for potassium-ion hybrid capacitors via regulating electrolyte

solvation structure, Angew Chem Int. Ed. 60 (2021) 26246–26253, https://doi.org/10.1002/anie.202112090.
[5] H. Wang, X. Chen, J. Zhang, Z. Yuan, P. Ye, J. Shen, Y. Zhong, Y. Hu, Unveiling the cooperative roles of pyrrolic-N and carboxyl groups in biomass-derived hierarchical porous carbon nanosheets for high energy-power Zn-ion hybrid supercapacitors, Appl. Surf. Sci. 598 (2022), 153819, https://doi.org/10.1016/j.apsusc.2022.153819.
[6] X. Zhao, J. Yan, H. Hong, Y. Zhao, Q. Li, Y. Tang, J. He, Z. Wei, S. He, X. Hou, C. Zhi, H. Li, Ligand-Substitution Chemistry Enabling Wide-Voltage Aqueous Hybrid Electrolyte for Ultrafast-Charging Batteries, Adv. Energy Mater. 45 (2022) 2202478, https://doi.org/10.1002/aenm.202202478.
[7] Y. Liu, H. Tan, Z. Tan, X. Cheng, Rice husk-derived carbon materials for aqueous Zn-ion hybrid supercapacitors, Appl. Surf. Sci. 608 (2023), 155215, https://doi.org/10.1016/j.apsusc.2022.155215.
[8] H. Wang, M. Wang, Y. Tang, A novel zinc-ion hybrid supercapacitor for long-life and low-cost energy storage applications, Energy Storage Mater. 13 (2018) 1–7, https://doi.org/10.1016/j.ensm.2017.12.022.
[9] Z. Zhou, X. Zhou, M. Zhang, S. Mu, Q. Liu, Y. Tang, In situ two-step activation strategy boosting hierarchical porous carbon cathode for an aqueous Zn-based hybrid energy storage device with high capacity and ultra-long cycling life, Small 16 (2020) e2003174.
[10] Z. Fan, J. Jin, C. Li, J. Cai, C. Wei, Y. Shao, G. Zou, J. Sun, 3D-printed Zn-ion hybrid capacitor enabled by universal divalent cation-gelated additive-free Ti_3C_2 MXene ink, ACS Nano 15 (2021) 3098–3107, https://doi.org/10.1021/acsnano.0c09646.
[11] Z. Zhai, L. Zhang, T. Du, B. Ren, Y. Xu, S. Wang, J. Miao, Z. Liu, A review of carbon materials for supercapacitors, Mater. Des. 221 (2022), 111017, https://doi.org/10.1016/j.matdes.2022.111017.
[12] A. Sohan, P. Banoth, M. Aleksandrova, A. Nirmala Grace, P. Kollu, Review on MXene synthesis, properties, and recent research exploring electrode architecture for supercapacitor applications, Int. J. Energy Res. 45 (2021) 19746–19771, https://doi.org/10.1002/er.7068.
[13] C. Yue, B. Hu, W. Huang, A. Liu, Z. Guo, J. Mu, X. Zhang, X. Liu, H. Che, Construction of polypyrrole nanowires@cobalt phosphide nanoflakes core–shell heterogeneous nanostructures as high-performance electrodes for supercapacitors, J Electroanal. Chem. 899 (2021), 115656, https://doi.org/10.1016/j.jelechem.2021.115656.
[14] X. Zheng, Y. Zhou, X. Yan, K. Lam, X. Hou, Vanadium Oxide with Elevated Interlayers for Durable Aqueous Hybrid Li^+/Zn^{2+} Batteries, ACS Appl. Energy Mater. 5 (7) (2022) 9070–9078, https://doi.org/10.1021/acsaem.2c01512.
[15] Y. Lu, Z. Li, Z. Bai, H. Mi, C. Ji, H. Pang, C. Yu, J. Qiu, High energy-power Zn-ion hybrid supercapacitors enabled by layered B/N co-doped carbon cathode, Nano Energy 66 (2019), 104132, https://doi.org/10.1016/j.nanoen.2019.104132.
[16] Q. Wang, S. Wang, X. Guo, L. Ruan, N. Wei, Y. Ma, J. Li, M. Wang, W. Li, W. Zeng, MXene-reduced graphene oxide aerogel for aqueous zinc-ion hybrid supercapacitor with ultralong cycle life, Adv. Electro. Mater. 5 (2019) 1900537, https://doi.org/10.1002/aelm.201900537.
[17] N.R. Chodankar, H.D. Pham, A.K. Nanjundan, J.F.S. Fernando, K. Jayaramulu, D. Golberg, Y.K. Han, D.P. Dubal, True meaning of pseudocapacitors and their performance metrics: Asymmetric versus hybrid supercapacitors, Small 16 (2020) e2002806.
[18] Q. Jiang, N. Kurra, M. Alhabeb, Y. Gogotsi, H.N. Alshareef, All pseudocapacitive MXene-RuO_2 asymmetric supercapacitors, Adv. Energy Mater. 8 (2018) 1703043, https://doi.org/10.1002/aenm.201703043.
[19] Z. Huang, T. Wang, H. Song, X. Li, G. Liang, D. Wang, Q. Yang, Z. Chen, L. Ma, Z. Liu, B. Gao, J. Fan, C. Zhi, Effects of anion carriers on capacitance and self-discharge behaviors of zinc ion capacitors, Angew Chem Int. Ed. 60 (2021) 1011–1021, https://doi.org/10.1002/anie.202012202.
[20] X. Ma, J. Cheng, L. Dong, W. Liu, J. Mou, L. Zhao, J. Wang, D. Ren, J. Wu, C. Xu, F. Kang, Multivalent ion storage towards high-performance aqueous zinc-ion hybrid supercapacitors, Energy Storage Mater. 20 (2019) 335–342, https://doi.org/10.1016/j.ensm.2018.10.020.
[21] X. Ma, J. Wang, X. Wang, L. Zhao, C., Xu, Aqueous V_2O_5/activated carbon zinc-ion hybrid capacitors with high energy density and excellent cycling stability, J. Mater. Sci.: Mater. Electron. 30 (2019) 5478–5486, https://doi.org/10.1007/s10854-019-00841-z.
[22] P. Zhu, P.R. Slater, E. Kendrick, Insights into architecture, design and manufacture of electrodes for lithium-ion batteries, Mater. Des. 223 (2022), 111208, https://doi.org/10.1016/j.matdes.2022.111208.
[23] Y. Ding, Y. Xin, Q. Zhang, Y. Zou, Acrylic resins with oxetane pendant groups for free radical and cationic dual-curing photoresists, Mater. Des. 213 (2022), 110370, https://doi.org/10.1016/j.matdes.2021.110370.
[24] H. Wei, Z. Xia, D. Xia, One step synthesis of uniform SnO_2 electrode by UV curing technology toward enhanced lithium-ion storage, ACS Appl. Mater. Interfaces 9 (2017) 7169–7176, https://doi.org/10.1021/acsami.6b15820.
[25] H. Wang, W. Ye, Y. Yang, Y. Zhong, Y. Hu, Zn-ion hybrid supercapacitors: Achievements, challenges and future perspectives, Nano Energy 85 (2021), https://doi.org/10.1016/j.nanoen.2021.105942.
[26] G. Kresse, J. Furthmüller, Efficient iterative schemes for ab initio total-energy calculations using a plane-wave basis set, Phys. Rev. B 54 (1996) 11169–11186, https://doi.org/10.1103/physrevb.54.11169.
[27] J.P. Perdew, K. Burke, M. Ernzerhof, Generalized gradient approximation made simple, Phys. Rev. Lett. 77 (1996) 3865–3868, https://doi.org/10.1103/PhysRevLett.77.3865.
[28] P.E. Blöchl, Projector augmented-wave method, Phys. Rev. B 50 (1994) 17953–17979, https://doi.org/10.1103/physrevb.50.17953.
[29] X. Liu, Z. Wang, Y. Niu, C. Liu, H. Chen, X. Ren, Z. Liu, W.-M. Lau, D. Zhou, Electrospun $_V2_O3$@carbon nanofibers as a flexible and binder-free cathode for highly stable aqueous Zn-ion full batteries, ACS Appl. Energy Mater. 5 (2022) 3525–3535, https://doi.org/10.1021/acsaem.1c04068.
[30] J.S. Park, S. Yang, Y.C. Kang, Boosting the electrochemical performance of V_2O_3 by anchoring on carbon nanotube microspheres with macrovoids for ultrafast and long-life aqueous zinc-ion batteries, Small Methods 5 (2021) e2100578.
[31] X. Liu, Z. Wang, Y. Niu, C. Liu, H. Chen, X. Ren, M. Wang, W.-M. Lau, D. Zhou, Scalable synthesis of novel V_2O_3/carbon composite as advanced cathode material for aqueous zinc-ion batteries, Ceram. Int. 48 (11) (2022) 15594–15602, https://doi.org/10.1016/j.ceramint.2022.02.093.
[32] D. Zhang, C. Zhang, Y. Zhao, X. Zheng, X. Shi, M. Yan, Y. Li, G. Liu, X. Liu, C. Yu, Facilely fabricating V_2O_3@C nanosheets grown on rGO as high-performance negative materials for lithium-ion batteries by adjusting surface tension, Int. J. Energy Res. 61 (2022) 12600–12608, https://doi.org/10.1021/acs.iecr.2c02032.
[33] S. Huang, S. He, H. Qin, X. Hou, Oxygen Defect Hydrated Vanadium Dioxide/Graphene as a Superior Cathode for Aqueous Zn Batteries, ACS APPL. Mater. Interfaces 13 (37) (2021) 44379–44388, https://doi.org/10.1021/acsami.1c12653.
[34] S. Yang, G. Yuan, W. Qiao, J. Bai, G. Wang, J. Yan, Vanadium acid zinc induced by electrochemical self-optimization of oxygen-defect-rich vanadium trioxide with dual-types of carbon hybridization for accelerating zinc storage dynamics, Electrochim. Acta 426 (2022), 140753, https://doi.org/10.1016/j.electacta.2022.140753.
[35] Z. Zhang, B. Xi, X. Wang, X. Ma, W. Chen, J. Feng, S. Xiong, Oxygen defects engineering of $VO_2{\cdot}xH_2O$ nanosheets via in situ polypyrrole polymerization for efficient aqueous zinc ion storage, Adv. Funct. Mater. 31 (2021) 2103070, https://doi.org/10.1002/adfm.202103070.
[36] H. Fan, X. Hu, S. Zhang, Z. Xu, G. Gao, Y. Zheng, G. Hu, Q. Chen, T.S. AlGarni, R. Luque, Flower-like carbon cathode prepared via in situ assembly for Zn-ion hybrid supercapacitors, Carbon 180 (2021) 254–264, https://doi.org/10.1016/j.carbon.2021.04.093.
[37] A. Amiri, M. Naraghi, A.A. Polycarpou, Zinc-ion hybrid supercapacitors with ultrahigh areal and gravimetric energy densities and long cycling life, J. Energy Chem. 70 (2022) 480–491, https://doi.org/10.1016/j.jechem.2022.03.029.
[38] S. Chen, L. Ma, K. Zhang, M. Kamruzzaman, C. Zhi, J.A. Zapien, A flexible solid-state zinc ion hybrid supercapacitor based on co-polymer derived hollow carbon spheres, J. Mater. Chem. A 7 (2019) 7784–7790, https://doi.org/10.1039/c9ta00733d.
[39] S. Wang, Q. Wang, W. Zeng, M. Wang, L. Ruan, Y. Ma, A new free-standing aqueous zinc-Ion capacitor based on MnO_2-CNTs cathode and MXene anode, Nano-Micro Lett. 11 (2019) 70, https://doi.org/10.1007/s40820-019-0301-1.
[40] H. He, J. Lian, C. Chen, Q. Xiong, C.C. Li, M. Zhang, Enabling multi-chemisorption sites on carbon nanofibers cathodes by an in-situ exfoliation strategy for high-performance Zn-ion hybrid capacitors, Nano-Micro Lett. 14 (2022) 106, https://doi.org/10.1007/s40820-022-00839-z.
[41] K. Yang, L. Hu, Y. Wang, J. Xia, M. Sun, Y. Zhang, C. Gou, C. Jia, Redox-active sodium 3,4-dihydroxy anthraquinone-2-sulfonate anchored on reduced graphene oxide for high-performance Zn-ion hybrid capacitors, J. Mater. Chem. A 10 (2022) 12532–12543, https://doi.org/10.1039/d2ta02630a.
[42] H. Luo, B. Wang, F. Wang, J. Yang, F. Wu, Y. Ning, Y. Zhou, D. Wang, H. Liu, S. Dou, Anodic oxidation strategy toward structure-optimized V_2O_3 cathode via electrolyte regulation for Zn-ion storage, ACS Nano 14 (2020) 7328–7337, https://doi.org/10.1021/acsnano.0c02658.
[43] G. Wang, Y. Wang, B. Guan, J. Liu, Y. Zhang, X. Shi, C. Tang, G. Li, Y. Li, X. Wang, L. Li, Hierarchical K-birnessite-MnO_2 carbon framework for high-energy-density and durable aqueous zinc-ion battery, Small 17 (2021) e2104557.
[44] X. Wang, Z. Zhang, M. Huang, J. Feng, S. Xiong, B. Xi, In situ electrochemically activated vanadium oxide cathode for advanced aqueous Zn-ion batteries, Nano Lett. 22 (2022) 119–127, https://doi.org/10.1021/acs.nanolett.1c03409.
[45] H. Duan, Z. Song, L. Miao, L. Li, D. Zhu, L. Gan, M. Liu, Unraveling the role of solvent–precursor interaction in fabricating heteroatomic carbon cathode for high-energy-density Zn-ion storage, J. Mater. Chem. A 10 (2022) 9837–9847, https://doi.org/10.1039/d2ta00754a.
[46] X. Zheng, L. Miao, Z. Song, W. Du, D. Zhu, Y. Lv, L. Li, L. Gan, M. Liu, In situ nanoarchitecturing of conjugated polyamide network-derived carbon cathodes toward high energy-power Zn-ion capacitors, J. Mater. Chem. A 10 (2022) 611–621, https://doi.org/10.1039/d1ta07350h.